

DECONVOLVING X-RAY SPECTRAL VARIABILITY COMPONENTS IN THE SEYFERT 1.5 NGC 3227

P. ARÉVALO

Pontificia Universidad Católica de Chile, Instituto de Astrofísica, Casilla 306, Santiago 22, Chile

A. MARKOWITZ

Center for Astrophysics and Space Sciences, University of California, San Diego, Mail Code 0424, La Jolla, CA 92093-0424, USA
Draft version May 8, 2021

ABSTRACT

We present the variability analysis of a 100 ks *XMM-Newton* observation of the Seyfert 1.5 active galaxy NGC 3227. The observation found NGC 3227 in a period where its hard power-law component displayed remarkably little long-term variability. This lucky event allows us to observe clearly a soft spectral component undergoing a large-amplitude but slow flux variation. Using combined spectral and timing analysis we isolate two independent variable continuum components and characterize their behavior as a function of timescale. Rapid and coherent variations throughout the 0.2–10 keV band reveal a spectrally hard (photon index $\Gamma \sim 1.7 - 1.8$) power law, dominating the observed variability on timescales of 30 ks and shorter. Another component produces coherent fluctuations in 0.2–2 keV range and is much softer ($\Gamma \sim 3$); it dominates the observed variability on timescales greater than 30 ks. Both components are viewed through the same absorbers identified in the time-averaged spectrum.

The combined spectral and timing analysis breaks the degeneracy between models for the soft excess: it is consistent with a power-law or thermal Comptonized component, but not with a blackbody or an ionized reflection component. We demonstrate that the rapid variability in NGC 3227 is intrinsic to continuum-emitting components and is not an effect of variable absorption.

Subject headings: Galaxies: active – galaxies: individual (NGC 3227) – X-rays: galaxies

1. INTRODUCTION

There is general consensus that the X-ray continuum emission in Seyfert Active Galactic Nuclei (AGN) and black hole X-ray Binaries (BH XRBs) is mainly produced by Compton up-scattering of lower energy photons in a hot ($\sim 10^9$ K) corona; these seed photons are likely produced thermally by the accretion disc which feeds the supermassive black hole (Haardt & Maraschi 1991). The resulting Comptonized spectrum is a power law with high- and low- energy cut-offs constrained, respectively, by the temperature of the Comptonizing medium and by the energies of the seed photon population (Sunyaev & Titarchuk 1980). Many Seyfert AGN spectra however exhibit an additional spectral component in the X-ray regime that manifests itself as an excess of emission over the power-law continuum below approximately 1 keV (Turner & Pounds 1989). The interpretation of the so-called soft excess is still a matter of debate, with models such as thermal Comptonization (Mehdipour et al. 2011), relativistically-blurred reflection off ionized gas (e.g. Ross & Fabian 2005; Crummy et al. 2006), or absorption (Gierliński & Done 2004) frequently invoked to model the soft emission.

In this paper we explore the X-ray continuum emission components originating in the accretion disk/Comptonization corona of the Seyfert 1.5 AGN NGC 3227 ($z=0.00386$; de Vaucouleurs & et al. 1991); we combine energy spectral fitting with variability analysis to deconvolve the X-ray spectral components that vary coherently.

Markowitz et al. (2009, hereafter M09) modeled in de-

tail the X-ray energy spectrum of NGC 3227 using a long look (100 ks continuous) observation with the *XMM-Newton* observatory. They modeled a continuum composed of a hard ($\Gamma \sim 1.6$) power law dominating the 1–10 keV band and a moderate soft excess below 1 keV. The soft excess was modeled approximately equally well by a simple steep ($\Gamma \sim 3.4$) power law, a Comptonized spectrum resulting from scattering off optically-thick ($\tau \sim 24$) gas with electron temperature ~ 0.35 keV, or a phenomenological blackbody component with temperature $k_B T \sim 0.08$ keV. A further complication is the presence of at least three zones of absorbing gas lying along the sight. These include a layer of cold absorption with column density $N_{\text{H,cold}} \sim 5 - 9 \times 10^{20} \text{ cm}^{-2}$ plus two ionized absorbers, one a lowly-ionized ($\log(\xi, \text{erg cm s}^{-1}) \sim 1.2 - 1.4^1$) absorber outflowing at $\sim 400 \text{ km s}^{-1}$ relative to the systemic velocity, the other more highly-ionized ($\log(\xi) \sim 2.9$) and outflowing at $\sim 2100 \text{ km s}^{-1}$ relative to systemic; both ionized zones had column densities $\sim 1 - 2 \times 10^{21} \text{ cm}^{-2}$. A way to tackle the model degeneracy is to combine the spectral analysis with analysis of the source variability as a function of energy band. The goal is to shed light on the possible connections between the continuum emission components, and importantly, on the (not yet fully-understood) emission and variability mechanisms.

The rest of this paper is organized as follows: §2 sum-

¹ $\xi \equiv L_{\text{ion}}/(nr^2)$, where L_{ion} is the luminosity of the ionizing continuum, n is the number density of the gas, and r is the distance from the source of the ionizing continuum to the gas cloud. All values of ξ in this paper are in quoted in units of erg cm s^{-1} .

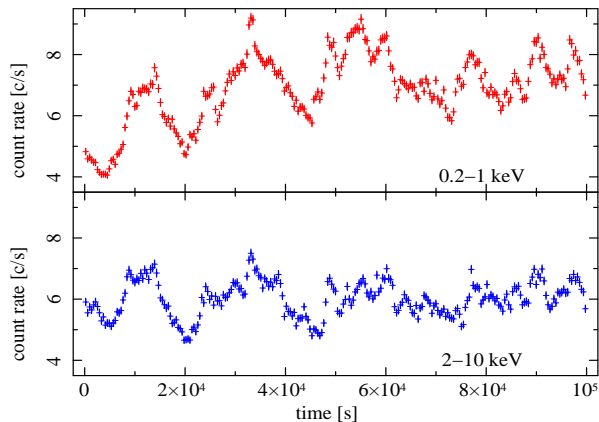


Figure 1. *XMM-Newton* EPIC light curves of NGC 3227 in soft (0.2–1 keV) and hard (2–10 keV) energy bands. The soft band displays higher amplitude of rapid fluctuations and a long term trend not visible in the hard band. We summarize the observations and light curve extraction. In §3, we use the new data to re-measure the 2–10 keV power density spectrum (PDS) for this source, previously published by Uttley & McHardy (2005, hereafter UM05). In §4, we compare variability trends in soft and hard bands over various timescales and measure interband coherence functions. We examine the energy spectra of the variable components in §5 and 6. We interpret the spectral components in the context of previous observations and comparison to other sources in §7. A summary of our main results is given in §8.

2. OBSERVATIONS AND LIGHT CURVE EXTRACTION

We used data from a *XMM-Newton* full-orbit observation of NGC 3227 taken on 2006 December 3–4 (obsID 0400270101). These data have been previously presented in M09, where the analysis was focused on energy spectral fitting. In this paper we consider data only from the EPIC pn detector and the focus of the analysis is on the variability properties of the light curves.

The EPIC pn camera (Strüder et al. 2001) was operated in Large Window mode, using the medium filter. Single and double events were extracted from a circular region of $40''$ radius centered on NGC 3227 and background photons were extracted from a source-free region of the equal area on the same chip. Only quality flag=0 photons were selected for both source and background. As noted by M09, pile-up on these pn data is negligible. The background-subtracted, 0.2–10 keV average count rate in the pn observation was $11.7 \text{ count s}^{-1}$.

Light curves were constructed in several energy bands as described in the analysis below. The count rates were corrected for dead time in each time bin, according to the good time interval file of the corresponding chip. Light curves for the soft (0.2–1 keV) and hard (2–10 keV) energy bands are displayed in Fig. 1.

3. POWER DENSITY SPECTRUM ANALYSIS

The broadband timing properties of NGC 3227 have been studied previously by UM05, who used data from four multi-timescale monitoring campaigns from the *Ross X-ray Timing Explorer* (*RXTE*), plus a long-look from *EXOSAT*. These campaigns consisted of regularly-spaced ~ 1 -ks snapshots, with sampling patterns and

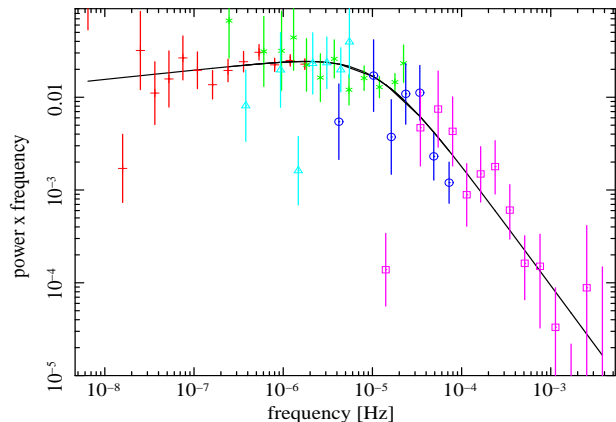


Figure 2. PDS data are denoted by points with error bars. The PDSs are unfolded and plotted in “model space”, i.e., plotted relative to the best-fit bending power-law model (solid line) and with the effects of Poisson noise and PDS measurement distortion effects removed. The red, green, cyan, and blue points denote the PDS segments derived from the “long-term”, “six-hourly”, “daily” and “long-look” *RXTE* campaigns, respectively (see UM05 for details of observations for each campaign). The *XMM-Newton* data are represented by the pink squares, covering the high frequency region. Notice the unusually low variability power of the lowest frequency *XMM-Newton* data point.

durations chosen such that the campaigns probe complementary ranges in temporal frequency space. This yielded a 2–10 keV power density spectrum (PDS) spanning from $\sim 7 \times 10^{-9}$ to $\sim 3 \times 10^{-3}$ Hz. UM05 fit a bending power-law model, $P(f) = Af^{\alpha_L} [1 + (f/f_b)^{\alpha_L - \alpha_H}]^{-1}$, where f_b is the bend frequency, α_L and α_H are the power-law slopes below and above f_b , respectively, and A is a normalization factor. They found a bend at $f_b = 2.6^{+6.1}_{-1.8} \times 10^{-5}$ Hz, with best-fit values of $\alpha_L = -1.0 \pm 0.1$ and $\alpha_H < -2.0$. Strong energy dependence was evident from the normalizations of the sub-band PDSs, where the lower energy band (3–5 keV) varied more strongly than the 7–15 keV band.

We used the EPIC light curves to both recalculate the high-frequency section of the PDS and investigate the energy dependence of variability amplitude extending to below 2 keV. For the former, we used the same *RXTE* Proportional Counter Array (PCA) data as in UM05, and extracted 2–10 keV lightcurves using standard extraction techniques (see e.g., Markowitz et al. 2003 or UM05) and the “pca.bkgd.cmffaint17_eMv20051128.mdl” PCA background files. We combined the PDS derived from the 2–10 keV *XMM-Newton* light curve with those derived from the “long-term”, “six hourly”, “daily,” and “long-look” *RXTE* campaigns described in UM05. The only difference is that the “long-term” campaign published in UM05 contained monitoring data from 1999 Jan 2 to 2005 Feb 24, but here we used monitoring up until 2005 Dec 4. We binned the periodograms using a minimum of 2 points per bin and a frequency binning of $\Delta f = 1.5f$. We used the PSRESP method (Uttley et al. 2002) to model the PDS with a bending power law; the observed PDS and best-fit model are shown in Fig. 2. This unfolded power spectrum is Poisson Noise-subtracted and the distortion effects caused by aliasing and red-noise leak have been removed.

Our best-fit bend frequency is $1.15^{+0.76}_{-0.81} \times 10^{-5}$ Hz,

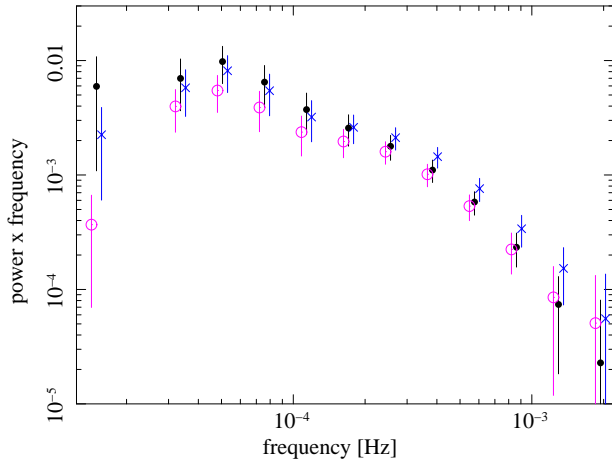


Figure 3. Power spectra calculated using only the *XMM-Newton* lightcurves in the soft band, 0.2–1 keV (black, filled circles), medium band, 1–2 keV (blue crosses) and hard band, 2–10 keV band (magenta open circles). The 1–2 keV points have been shifted slightly to lower frequencies and the 2–10 keV point to higher frequencies to avoid overlapping error bars.

consistent with UM05. The high-frequency slope is $\alpha_H < -2.0$, where errors quoted correspond to 68% bounds. For the low-frequency slope, the best-fit value was $\alpha_L = -0.9$, with uncertainties pegging at the boundaries of the range over which we tested α_L , -0.8 to -1.0 (the current PDS does not offer any ability for us to constrain the low-frequency shape of the PDS any better than UM05, so we restricted α_L to encompass the best-fit values from UM05). The *XMM-Newton* PDS data, plotted in pink in Fig. 2, show that for this *XMM-Newton* light curve the variability power at the longest timescales probed (~ 100 ks) is unusually low. Although this is not strange given the stochastic red noise behavior of AGN variability (Vaughan et al. 2003), it does give us the rare opportunity to study in detail the variability of components other than the hard power law. In the following sections we will attempt to disentangle the spectral components of the variability.

The power spectra of the *XMM-Newton* light curves were computed with the Mexican-hat procedure described in Arévalo et al. (2012). This method convolves the lightcurves with a band-pass filter and then computes the variance of the filtered lightcurve as a measure of the variability power as a function of variability timescale. The power spectrum was calculated for three energy bands, soft (0.2–1 keV), medium (1–2 keV) and hard (2–10 keV). Figure 3 shows these power spectra for each band in black filled circles, blue crosses and open magenta circles, respectively. The *XMM-Newton* power spectra taken on their own appear to have higher frequency breaks (near $\sim 5 \times 10^{-5}$ Hz) than the complete data set. This is probably an artifact of the unusually small amplitude of variability on the longest timescales of the *XMM-Newton* observation. At frequencies $\lesssim 5 \times 10^{-5}$ Hz, the amount of power in the three bands diverges sharply. We explore the energy dependence of the variability in further detail in the following sections.

4. INTERBAND CROSS-CORRELATION

As demonstrated in the previous section, the *XMM-Newton* light curves in different energy bands display qualitatively similar variability patterns but with different amplitudes on different timescales. In this section, we will investigate further the dependence of variability amplitudes on time scale and energy band and we will then investigate the degree of correlation between the variations in different energy bands.

We constructed light curves from the pn data for 22 energy bands in the 0.2–10 keV range. The energy resolution was chosen to allow similar number counts in each band, taking care to include integer numbers of pn energy channels. For the spectral fitting, the pn response matrix was re-binned using the same energy resolution of the light curves by using the task RBNRMF.

We isolated variability trends over various timescales in each light curve by applying a Mexican-hat type filter: in this method, described in Arévalo et al. (2012), one convolves each light curve with two Gaussian profiles, of slightly different widths, and takes the difference of the convolved light curves. This convolution and difference procedure is equivalent to a multiplication of the power spectrum by a filter which peaks at a frequency equal to $0.225/\sigma$. This method thus isolates variations on timescales of $\sigma/0.225$ where σ is the average width of the Gaussian filters, effectively removing variations on shorter and longer timescales. Varying the value of σ we can isolate the variability pattern and amplitude as a function of filter timescale or equivalently, frequency, to construct filtered light curves and power spectra. This is particularly useful to remove effects of red-noise leak, which would hamper a Fourier analysis alternative to decompose the variability patterns at different timescales, especially for the low energy cases which show a strong trend on timescales longer than the observation. For the analysis below we used pairs of Gaussian kernels separate in width by a factor of 1.01 but the results are quite insensitive to the choice of width separation as explained in Arévalo et al. (2012).

We filtered the light curves with this procedure in two different timescales, 100 ks and 10 ks. In the top panel of Fig. 4, we plot the 100 ks trends for a range of selected energy bands. The softest energy bands have the largest amplitudes of fluctuations. Moreover, the pattern of variability changes above energies of 2 keV, providing evidence for two or more distinct spectral components. In the bottom panel, the rapid, 10 ks fluctuations in the same energy bands are shown. For these shorter timescales, all the energy bands from 0.2 to 10 keV show consistent fluctuation patterns.

Next, we quantified the coherence between energy bands by calculating the cross correlation function (CCF) between the filtered light curves for 100.3, 66.8, 44.6, 29.7, 19.8, 13.2, 8.8, and 5.9 ks, the eight timescales used to generate σ_{rms} spectra (described below). We chose an intermediate energy band (1.1–1.25 keV) as reference and computed the CCF between this band and each of the other bands. The CCF peak values as a function of energy band are plotted in Fig. 5.

The slower variations (timescales longer than ~ 40 ks) are fully coherent with the reference band up to energies of 2 keV. Above this energy, the light curves lose

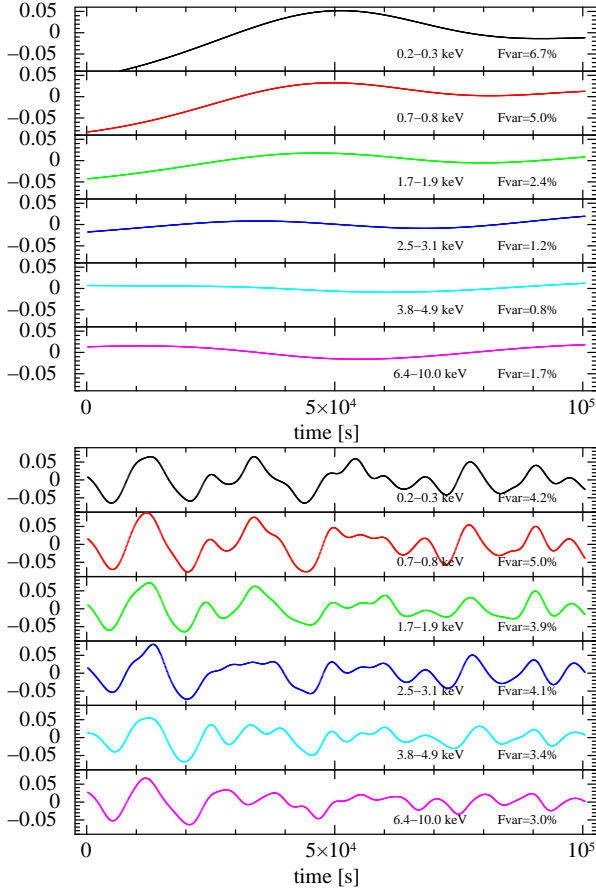


Figure 4. *Top panel:* Light curves in various energy bands filtered to show only long-term (100 ks) fluctuations; the variations change shape at energies around 2 keV. *Bottom panel:* light curves in the same energy bands, now filtered for shorter timescale fluctuations (5.9 ks). The variations remain coherent throughout the energy range.

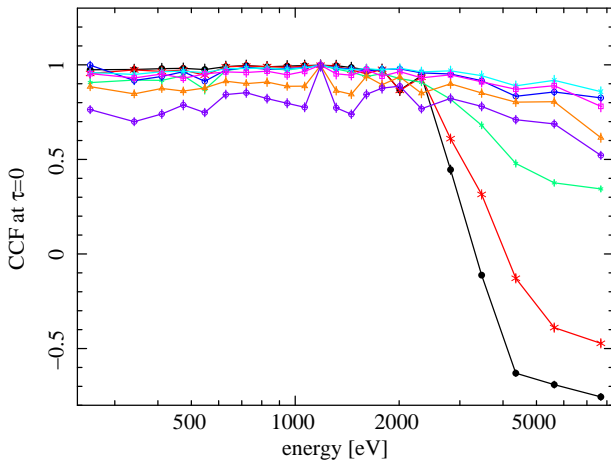


Figure 5. Coherence between the 1.1–1.25 keV light curve and variations in all other energy bands for fluctuations in eight timescales. Black, red, green, blue, cyan, magenta, orange and purple, probe variations on timescales of 100.3, 66.8, 44.6, 29.7, 19.8, 13.2, 8.8, and 5.9 ks, respectively. The CCF value at 0 time lag is plotted in the y-axis.

coherence with the variations in the reference band, approaching an anti-correlated trend with a central CCF value of almost -0.8 . The light curves are too short to establish whether this anti-correlation is significant or just a chance offset of half a cycle between uncorrelated light curves. It is clear, however, that for these long term trends, the variations are synchronized for all bands between 0.2 and 2 keV and above this energy the variability pattern changes. In contrast, rapid fluctuations (timescales ≤ 30 ks) are highly coherent throughout the energy range probed. This result indicates that one spectral component covers the 0.2–10 keV energy range and is varying coherently on these short timescales.

The rapid fluctuations are quasi-simultaneous across the whole energy range but there are small delays between different energy bands, as can be seen in the bottom panel of Fig. 4. The peak of the CCF function shifts slightly with increasing energy separation. For light curves filtered at timescales around 19.8 ks (corresponding to the cyan line in Fig. 5 and σ_{rms} spectrum #5 below), the CCF peaks at a maximum lag of 500 s between the reference band and the highest energy band. This time lag corresponds to about 2% of the variability timescale. Similar time lags, where the harder bands lag the softer ones, are commonly seen in the powerlaw component of Seyfert galaxies (e.g. Papadakis et al. 2001; Vaughan et al. 2003; McHardy et al. 2004; Markowitz & Uttley 2005; Arévalo et al. 2006, 2008b; Walton et al. 2013).

5. SPECTRA OF THE VARIABLE COMPONENTS

The coherence analysis shows that the difference in the soft and hard light curves in Fig. 4 arises from at least two spectral components varying on different timescales. Here we will explore in detail this energy dependence by determining the spectral shape of the variable components.

The spectral shape of the variable components can be studied using the σ_{rms} spectrum (Revnivtsev et al. 1999) where the flux at each energy bin is replaced by the amplitude of σ_{rms} fluctuations in the lightcurve of the corresponding energy band. We note that the stochastic nature of the X-ray lightcurves means that the power of any Fourier mode varies greatly from one observation to another around the underlying mean value. High-frequency modes can normally be binned together so that many modes fall in the same bin and the average value is always closer to the underlying power spectrum. Low-frequency modes are more sparse and only few modes can be binned together so the scatter between low frequency powerspectral points of different observations is large. The σ_{rms} spectrum is a collection of powerspectral estimates at a fixed frequency for different energy bands. If the energy bands are correlated, then a simultaneous observation will catch them all in the same fluctuation, so that if in our particular observation the power-spectrum estimate is higher/lower than the average it will be so for all the energy bins. Therefore, for energy bands that vary in a correlated way, even a single Fourier mode can be used to calculate the *shape* of the σ_{rms} spectrum, even if the *normalization* is uncertain due to the stochastic nature of the light curves. Another

consequence of the simultaneity of the observations is that the point-to-point scatter between σ_{rms} spectrum bins is produced by the uncorrelated variability only, i.e. the Poisson noise and additional small amplitude variable components that might affect one band more than others, not by the stochastic nature of the intrinsic variability.

We constructed σ_{rms} spectra by calculating σ_{rms} variability amplitudes for band-pass-filtered lightcurves as a function of energy. The result is the spectral shape of all components that vary on that particular timescale, i.e. the σ_{rms} spectrum. As a reminder, the energy spectrum describes the distribution of emitted/absorbed photons as a function of energy regardless of variability or lack thereof; the σ_{rms} spectrum, meanwhile, isolates the contributions from only those spectral components that are variable over a given timescale. Any constant additive components are automatically removed from the σ_{rms} spectra while constant multiplicative components appear with the same shape as in a flux spectrum. Variable multiplicative components, such as variable absorption, produce peaks in the σ_{rms} spectrum at energies where they produce the largest changes, normally where the absorption is strongest and dips would appear in the flux spectrum. One can calculate and fit σ_{rms} spectra and compare to those components modeled in the time-averaged energy spectrum to determine which component(s) are relevant to explaining observed variability for a given timescale/temporal frequency range.

We thus repeated the filtering procedure with different values of σ to track the evolution of the σ_{rms} spectrum with variability timescale. We probe in total eight timescales ranging from 100 ks (henceforth referred to as #1) down to 5.9 ks (#8). The power of the Poisson noise in each light curve is estimated from the light curve error bars, which incorporate the uncertainties due to counting noise of the photons in the source and background time bins. For the power spectrum normalization used here, the Poisson noise power $\text{PN} = 1/(\text{err}^2 \times dt)$, where dt is the time bin in s and err is the average error of the lightcurve bins. The Poisson noise is white noise and therefore its contribution is the same at every temporal frequency. This estimate of the power due to Poisson noise is thus subtracted from the variance measurement at each timescale and the process is repeated for each energy band. We note that since all the energy bands have similar count rates their Poisson noise contributions are also similar. The resulting σ_{rms} spectra denote the intrinsic variability of each band, in units of $\text{count s}^{-1} \text{keV}^{-1}$. Higher frequency σ_{rms} spectra have lower intrinsic variability power so the Poisson noise contribution is relatively stronger. Therefore, the subtraction of Poisson noise power produces a larger uncertainty in higher frequency σ_{rms} spectra and for this reason they have larger error bars.

As can be seen in Fig. 5, different energy bands are highly correlated but the correlation is not perfect. This is partly due to the uncorrelated contribution of Poisson noise to each band and partly an effect of minor spectral component displaying uncorrelated variations. These additional sources of variability introduce power to some bins in the σ_{rms} spectrum that add to the σ_{rms} power of

the fully coherent fluctuations of a single spectral component. Since it is not clear *a priori* which energy bins are carrying the uncorrelated source of variability, it is not possible to subtract this contribution, but it is possible to incorporate its average effect on the errors. We used the drop in coherence between energy bands to estimate the contribution of uncorrelated fluctuations (Poisson and intrinsic) to the variability at each timescale. We then introduced this contribution as uncorrelated error in the corresponding σ_{rms} spectra, knowing that the true correlated σ_{rms} power must be within this value of the measured power.

Two of the σ_{rms} spectra, #1 and #5, are plotted in Fig. 6, to illustrate the change in spectral shape with timescale. Spectrum #1 correspond to the slowest fluctuations, where the difference between soft and hard light curves is strongest. Spectrum #5 is characteristic of the more rapid fluctuations — at this frequency and above the fluctuations of the entire energy range are well correlated. Also plotted is the time-averaged spectrum, degraded to match the resolution of the σ_{rms} spectra.

For all spectral fitting, we used XSPEC version 12.8.0; uncertainties on best-fit model parameters correspond to $\Delta\chi^2 = +2.71$ (90% confidence for one parameter) unless otherwise noted. As a preliminary step, we fit the three spectra with a crude model consisting solely of a simple power law. This model and all models discussed herein contain neutral absorption due to the Galactic column, $1.98 \times 10^{20} \text{ cm}^{-2}$ (Kalberla et al. 2005), modeled with PHABS. Data/model residuals are plotted in the lower panel of Fig. 6

Spectrum #1 was fit only in the 0.2–4 keV range, and there is a strong increase in variability power above the extrapolation of the power law. This does not mean, however, that the soft spectral component has an upturn at high energies. From the coherence analysis it is clear that above ~ 2 keV, a different spectral component begins to dominate the variability, so that by ~ 5 keV the fluctuations are uncorrelated to the soft component.

This behavior is consistent with the two-component interpretation, where the components are varying incoherently on long timescales with different amplitudes. At low energies the variability is dominated by the large amplitude of the soft component variations, but in higher energy bands this soft component is weak, so the low-amplitude variability of the hard component takes over. Near 2 keV, where the coherence changes from 1 to -0.8 , the variations interfere, since the value of the coherence coefficient of -0.8 indicates that the fluctuations of both components are almost exactly out of phase. Therefore, the variance in these intermediate bands that have similar amplitude contributions from soft and hard components is reduced, producing an artificial dip in the σ_{rms} spectrum. The coherent variability from 0.2 to 2 keV however ensures that the σ_{rms} spectrum in this energy range can be interpreted as a single component that truly reflects the shape of the emitted spectrum. Above this energy we can expect contributions from two or more spectral components whose variations interfere, distorting the shape of the σ_{rms} spectrum. Below, we thus fit spectra #1–#3 only up to 3 keV; a simple power-law fit yields $\Gamma \sim 2.33$. As we will demonstrate below, spectrum

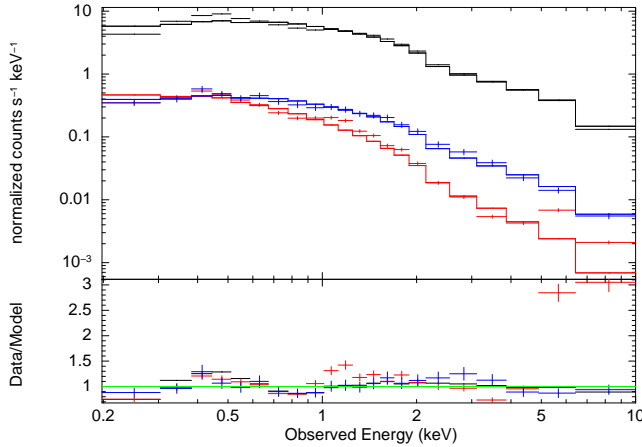


Figure 6. σ_{rms} variability spectra for low-frequency fluctuations (1×10^{-5} Hz; spectrum #1) in red and high-frequency fluctuations (5×10^{-5} Hz; spectrum #5) in blue, together with the time-averaged spectrum in black. The spectra are fitted with a simple power law affected only by neutral absorption due to the Galactic column. Spectrum #1 is fit only over 0.2–4 keV because above this energy the fluctuations are incoherent with those below about 2 keV.

#1 is fairly representative of spectra #1–#3,

Spectrum #5, meanwhile, is much flatter, with $\Gamma \sim 1.57$. Since fluctuations in this timescale are highly coherent throughout the entire energy range, the σ_{rms} spectrum can be more simply interpreted as a single physical spectral component. As will be demonstrated below, spectrum #5 is representative of spectra #4–#8.

6. MODEL FITS TO THE σ_{rms} SPECTRA

The continuum of the time-averaged spectrum is also modified by as-yet unmodeled line of sight absorption (M09), as evidenced by the dip near 0.8 keV. Models consisting of a simple power law are poor fits, with $\chi^2/\text{dof} = 201/16 = 12.5$ and $29.5/20 = 1.5$ for spectra #1 and #5, respectively. The data/model residuals for both σ_{rms} spectra are similar: there are ± 30 –40% deviations, significant curvature below 0.4 keV, and a strong dip near 0.7–0.9 keV, the energies most strongly affected by the low-ionization ($\log(\xi) \sim 1.2$ –1.5) absorber modeled in the EPIC and Reflection Grating Spectrometer (RGS) energy spectra by M09. We now demonstrate that the σ_{rms} spectra are consistent with being modified by the same absorbers while simultaneously exploring mechanisms to explain their form.

6.1. Low-frequency σ_{rms} spectra

We started with spectrum #1, re-plotted in Fig. 7. We added a full-covering neutral absorber with ZPHABS; χ^2/dof fell to $85.2/15 = 5.7$ for $\Gamma \sim 2.45$ and column density $N_{\text{H,cold}} \sim 3 \times 10^{20} \text{ cm}^{-2}$, but data/model residuals (Fig. 7b) were still poor. Finally, we modeled a full-covering zone of ionized absorption using the same XSTAR table as M09. Redshifts for all ionized absorbers were frozen at the values from fits to the time-averaged RGS spectrum in M09; all abundances were frozen at solar values. This fit yielded $\chi^2/\text{dof} = 27.9/13 = 2.15$, with best-fit parameters listed in Table 1, including $\Gamma = 3.03 \pm 0.17$, nearly consistent with that for the soft X-ray power-law

in the time-averaged spectrum. Data/model residuals (Fig. 7c) are generally acceptable except for two points at 1.1–1.25 keV, but there are no clear candidates for what causes this deviation. One might expect some Fe L edge absorption near 1.0–1.3 keV due to lowly- or moderately-ionized gas, but only at the $\sim 6\%$ level for the best-fit values of $\log(\xi)$ and column density $N_{\text{H,WA}}$; allowing the Fe abundance relative to solar vary had no effect on the fit.

The σ_{rms} spectrum is not highly sensitive to the higher-ionization ($\log(\xi) \sim 2.9$) absorber modeled in the EPIC and RGS energy spectra. This absorber affects the continuum only at the \sim few percent level. It also introduces discrete absorption lines, the strongest due to H-like O and Ne and He-like Fe, but the σ_{rms} spectrum lacks the energy resolution to detect them.

We tested if the continuum could also be modeled by thermal Comptonization, as per fits to the time-averaged EPIC spectrum. We replaced the power law with a COMPST component. The best-fit model (see Table 1) yielded data/model residuals virtually identical to those for the power-law, as the Comptonized component effectively resembles a power law, with a slight bend above ~ 2 keV. Best-fit parameters for optical depth τ and electron temperature $k_B T_e$ are factors of roughly ~ 2 lower and ~ 3 higher, respectively, than in M09. However, there exists some degeneracy between these two parameters, and they are anticorrelated in the direction of the best-fit values of M09.

Next, we replaced the COMPST component with a blackbody component, as M09 were able to model the soft excess with a phenomenological blackbody with temperature $k_B T \sim 83$ eV. However, this yielded an extremely poor fit ($\chi^2/\text{dof} = 595/13 \sim 46$ for $k_B T \sim 200$ eV; data/model residuals in Fig. 7d), and we conclude that an absorbed blackbody is not able to describe the variable component.

Finally, we also tested models incorporating reflection from an ionized medium, using REFLION (Ross & Fabian 2005), and tested both unblurred and blurred emission, the latter using KDBLUR. However, we did not achieve a satisfactory fit despite trying the fit with a wide range of initial parameters and with all parameters except outer radius of blurring left free; our best fit had $\chi^2_{\text{red}} \sim 12$ for a model with $\xi \sim 300 \text{ erg cm s}^{-1}$, inner radius of blurring $\sim 1 - 3R_g$ and an emissivity index q near 0. Adding the low-ionization warm absorber improved the fit quality only slightly, with $\chi^2_{\text{red}} \sim 9$ (best-fit parameters include $\xi \sim 400 \text{ erg cm s}^{-1}$, inclination angle ~ 85 degrees, inner radius of blurring $\sim 1 - 2R_g$). The very strong data/model residuals are plotted in Fig. 7e. Any model with significantly lower values of ξ had a spectral shape above 1 keV that was much too flat to match the observed spectrum. Adding in neutral absorption via ZPHABS did not significantly improve any of the above fits.

6.2. High-frequency σ_{rms} spectra

We now turn to spectrum #5, the higher-temporal frequency spectrum. We fit the 0.2–10 keV spectrum; the simple power-law model above yielded

$\chi^2/dof=29.5/20=1.5$ for $\Gamma \sim 1.57$. Data/model residuals (Fig. 6b) had a very similar shape to those for the low-frequency fit with a power law, indicating that similar zones of absorption may be appropriate to model. We tried modeling Compton reflection using the PEXRAV component, and using values from M09, but this had no effect on the fit due to the limited energy range of EPIC and is not discussed further. We added a warm absorber with $\log(\xi) \sim 0.6$; data/model residuals are plotted in Fig. 8b. χ^2/dof fell to $16.7/18=0.93$ i.e., already an acceptable fit. For completeness, however, and to improve residuals <0.4 keV, we added a neutral absorber to the model with PHABS and obtained our best-fit model; best-fit parameters are listed in Table 1 and data/model residuals are plotted in Fig. 8c. Γ is $1.87^{+0.15}_{-0.10}$, similar to that for the hard power-law component in the time-averaged spectrum. We will demonstrate in the discussion section that the hard spectral components in the σ_{rms} and time-averaged spectra are in fact consistent with each other, i.e., we confirm the hard X-ray power-law as the only variable component on these timescales.

To track the spectral slope and thus the dominating spectral component as a function of timescale, we simultaneously fit all eight σ_{rms} spectra with a model consisting of a power-law modified by the cold absorber and low-ionization warm absorber, with column densities each left free. The value of $\log(\xi)$ was fixed at 1.43. We included for completeness the high-ionization absorber with $\log(\xi)$ fixed at 2.89 and column density frozen at $1.5 \times 10^{21} \text{ cm}^{-2}$. The resulting values of Γ as a function of timescale are plotted in Fig. 9. A change in spectral slope occurs sharply at a variability timescale of 30 ks, close to the break frequency in the PDS. We conclude that a soft spectral component alone is producing the long-term trend seen through the *XMM-Newton* observation, while all the rapid fluctuations are produced by a hard power-law component with $\Gamma \sim 1.6 - 1.7$.

6.3. Variable cold absorption

We investigated if the observed smooth flux change affecting mainly the soft energy bands could be due to varying cold absorption, for example by a cloud crossing the line of sight on timescales of 100 ks. In this case, considering that the hard power law is not varying strongly on timescales of about 50 ks or longer, the low-frequency σ_{rms} spectrum should have the same shape as the difference between the spectra with initial and final absorption values. We explored this possibility by constructing difference spectra of variable cold absorption and comparing their shapes to that of the σ_{rms} spectrum of slow fluctuations.

The difference spectra were constructed by taking the best-fitting model to the time-averaged spectrum of M09, varying the value of $N_{\text{H,cold}}$ (henceforth simply N_{H} , with units of cm^{-2} for all values discussed) of the full-covering, cold absorber around its best-fitting value and taking the difference of model spectra with different values of N_{H} . If the observed slow/soft variability is produced only by a change in N_{H} then the σ_{rms} spectrum will have the same shape as the difference spectrum, although the normalization can be different. We fitted a simple power-

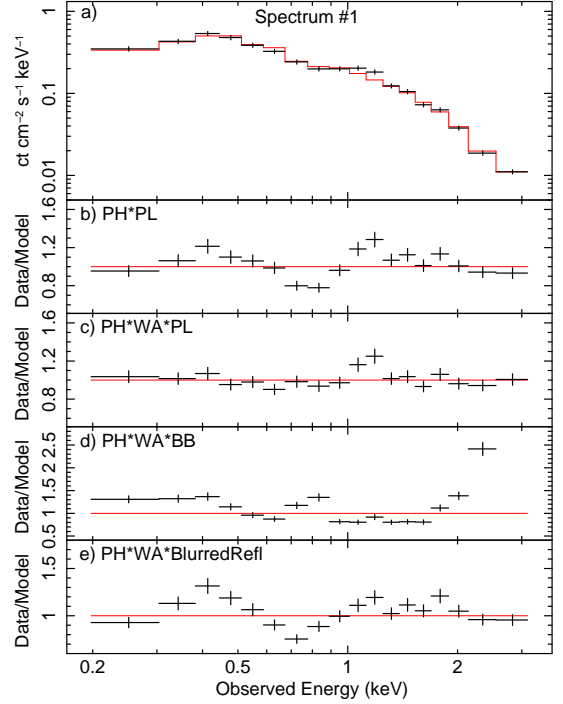


Figure 7. Spectral fits to the lowest-frequency σ_{rms} spectrum (#1; timescale of 100 ks). The top panel shows the data and best-fit model. Panel b shows the data/model residuals to a power-law modified by cold absorption (in excess of the Galactic column). Panel c shows the data/model residuals for the best-fit model, which includes the low-ionization warm absorber. In panel d, the power law has been replaced by a blackbody component; this yields a very poor fit. In panel e, the continuum emission is modeled by blurred reflection off an ionized medium; this also yields a very poor fit.

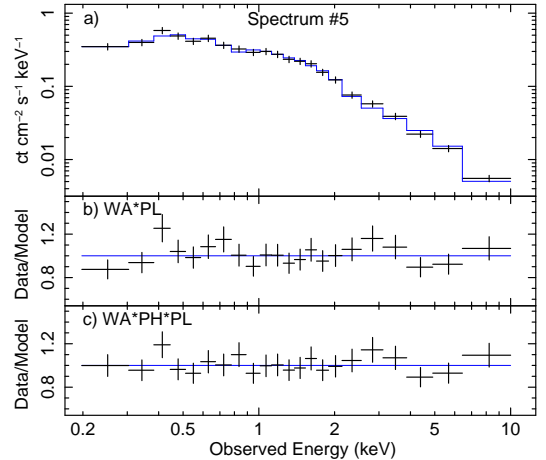


Figure 8. Spectral fits to the lowest-frequency σ_{rms} spectrum (#5; timescale of 19.8 ks). The top panel shows the data and best-fit model. Panel b shows the data/model residuals to a power-law modified by cold absorption (in addition to the Galactic column). Panel c shows the data/model residuals for the best-fit model, which includes both excess cold absorption and the low-ionization warm absorber.

Table 1
Model Fits to Low- and High-Frequency RMS Spectra

| | Low Frequency (power law) | Low Frequency (COMPST) | High Frequency (power law) |
|--|---------------------------------------|------------------------------------|------------------------------------|
| χ^2/dof | 27.9/13=2.15 | 26.7/12=2.22 | 10.9/17=0.64 |
| Γ | 3.03 ± 0.17 | | $1.87^{+0.15}_{-0.10}$ |
| A_1 (ph cm $^{-2}$ s $^{-1}$ keV $^{-1}$) | $3.60^{+0.65}_{-0.50} \times 10^{-4}$ | | $5.0^{+1.3}_{-0.9} \times 10^{-4}$ |
| $k_B T_e$ (keV) | | $1.0^{+8.0}_{-0.3}$ | |
| τ | | 14^{+4}_{-13} | |
| Norm. | | $3.5^{+0.6}_{-0.5} \times 10^{-4}$ | |
| N_H (neutral; 10^{20} cm $^{-2}$) | 6^{+3}_{-2} | 6 ± 3 | < 6.7 |
| N_H (ionized; 10^{21} cm $^{-2}$) | $2.0^{+0.6}_{-0.5}$ | $2.2^{+1.0}_{-0.6}$ | $3.0^{+7.0}_{-1.5}$ |
| $\log(\xi, \text{erg cm s}^{-1})$ | $0.85^{+0.25}_{-0.35}$ | $1.00^{+0.25}_{-0.40}$ | 1.35 ± 0.60 |

Note. — Model parameters for best fits to low- and high-frequency σ_{rms} spectra (#1 and #5, respectively). The reader is referred to the XSPEC help manual for the units of the normalization of the COMPST component. A_1 is the normalization of the power law at 1 keV.

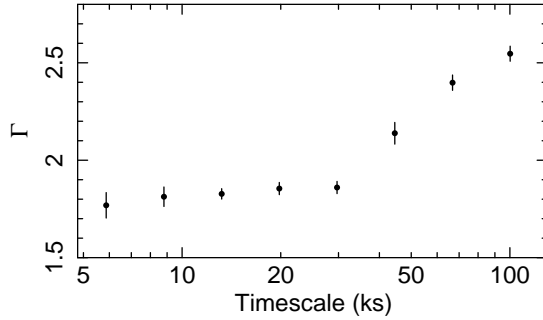


Figure 9. Best-fit values of photon index for each σ_{rms} spectrum as a function of variability timescale, and after accounting for line of sight absorption following M09. The spectrum of the variable component changes abruptly at a variability timescale of 30 ks, close to the break frequency in the power spectrum.

law model to the difference and σ_{rms} spectra tying together their photon indices and leaving their normalizations free. The ratio of these spectra to the best fitting power-law model highlights the difference between the spectra while correcting for their different normalizations. Since we are only interested in the comparison of the shape of the low-frequency σ_{rms} spectrum to the difference spectra produced by variable cold absorption, these ratio plots are sufficiently informative and a sample of difference spectra is shown in Fig. 10.

We started by calculating difference spectra with initial and final values of N_H of 3×10^{20} and 10×10^{20} , respectively. These straddle the best-fit time-averaged value of 7×10^{20} and produce the observed factor of two increase observed in the flux of the 0.2–1 keV light curve. We also tested different values of N_H covering a wider range but still straddling the time-averaged value, such as the $1\text{--}10 \times 10^{20}$ and $3\text{--}30 \times 10^{20}$ difference spectra plotted in Fig. 10 in orange and blue triangles, respectively.

All difference spectra investigated have a characteristic peak that deviates from a simple powerlaw significantly more than the observed σ_{rms} spectrum does. We therefore conclude that the slow trend seen in the soft light curve cannot be produced by a change in the N_H of a full-covering cold absorber.

Changes in partial covering are also unable to reproduce the shape of the σ_{rms} spectrum. We first con-

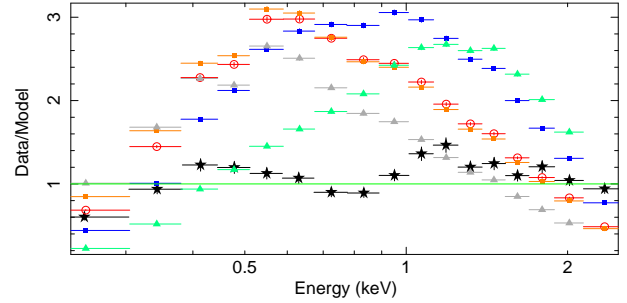


Figure 10. Comparison of the low-frequency σ_{rms} spectrum, denoted by black stars, to the difference spectra produced by variable full-covering cold absorption. The red open circles correspond to a change in N_H from 3 to 10×10^{20} cm $^{-2}$, encompassing the best-fit time-averaged value; orange and blue squares represent even larger changes in N_H still covering the time-averaged values of N_H . Triangles show cases of more extreme changes in N_H , with both initial and final values of N_H above (green) and below (grey) the time-averaged value. All spectra have been divided by a power-law model of equal slope to highlight the differences in their shapes. Evidently, varying the column of a full-covering absorber cannot explain the shape of the low-frequency σ_{rms} spectrum and therefore cannot be the cause of the slow trend in the soft band light curves.

structed difference spectra where the initial and final spectra were subject to partial covering of cold gas (using PCFABS in XSPEC), where the covering fraction varied but the column density $N_{H,PC}$ did not. The shape of these difference spectra only depends on the value of $N_{H,PC}$, not on the initial and final covering fractions. Only the normalization of these difference spectra is proportional to the difference in covering fraction. Since the normalization is modeled out by dividing the σ_{rms} and difference spectra by powerlaw models with their best-fitting normalization, variations in only one parameter need to be explored. The difference spectra of these variable-covering fraction models are plotted with circles in Fig. 11 for values of $N_{H,PC} = 5, 20$ and 80×10^{20} , plotted in red, blue, and purple circles, respectively. The value of $N_{H,PC}$ determines the position of the peak in the difference spectra compared to a simple power law, but the shape remains relatively constant, increasing much more steeply than the σ_{rms} spectrum below the peak and also decreasing much more steeply after. The final scenario we tested was a partial coverer whose column den-

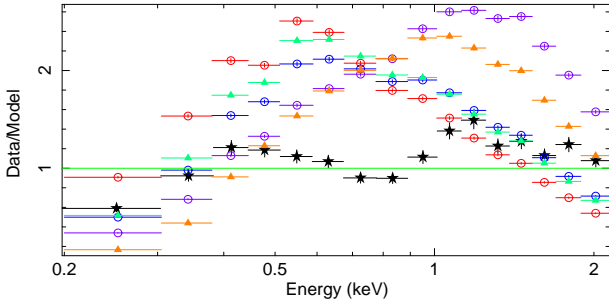


Figure 11. Comparison of the low-frequency σ_{rms} spectrum, in black stars, to the difference spectra produced by variable covering fractions, plotted in circles, and variable N_{H} for a 50 % covering fraction, plotted in triangles. The N_{H} values used for the variable covering fraction spectra were 5, 20 and 80×10^{20} , plotted in red, blue and purple circles. For the constant 50% covering fraction models we used N_{H} changing from 3 to 10×10^{20} (green triangles) and 10 to 30×10^{20} (orange triangles). A varying covering fraction or variable N_{H} of a partial coverer do not produce difference spectra that can explain the low-frequency σ_{rms} spectrum.

sity $N_{\text{H,PC}}$ varies while the covering fraction remains the same. The resulting difference spectra are qualitatively similar to those described above and a couple of examples are plotted in Fig. 11 in triangles, for a constant covering fraction of 50% and values of $N_{\text{H,PC}}$ changing from 3 to 10×10^{20} (green triangles) and 10 to 30×10^{20} (orange triangles). We conclude that a partial coverer with either varying covering fraction or variable column density does not produce difference spectra that can explain the observed low-frequency σ_{rms} spectrum or the smooth increase in soft band flux.

7. INTERPRETATION OF THE VARIABILITY SPECTRA

We have used coherence and Fourier-resolved spectral analysis to deconvolve two independently-varying continuum components: a soft spectral component consistent with a power law of Photon Index $\Gamma = 3.03 \pm 0.17$ that varies on timescales of 30–100 ks, and a hard power-law component of $\Gamma = 1.87 \pm 0.15$. The hard power law component accounts for variability across the entire energy range on all shorter timescales. In this section we will explore different possible scenarios to explain these components and their behavior during this observation and we compare our results to previous studies.

7.1. Slowly-varying soft component

The long-term trend, evident in the 0.2–1 keV light curve of Fig. 1, dominates the variance of the lowest frequency σ_{rms} spectra. The spectral shape corresponding to this fluctuation is very soft, and can be fitted with a power law of $\Gamma = 3.03 \pm 0.17$ plus neutral and warm absorption as demonstrated in Fig. 7.

The low frequency σ_{rms} spectrum is reminiscent of the soft excess component in the spectral fit to the time-averaged spectrum of NGC 3227 by Markowitz et al. (2009). The σ_{rms} spectrum can also be modeled well by a COMPST component with parameters roughly consistent to those in the time-averaged spectrum, also affected by warm absorption. The consistency between warm absorption parameters on the σ_{rms} and time-averaged spectra argues for a *constant* warm absorber acting on a soft excess of variable normalization. Thermal Comptoniza-

tion models have been successfully used to model soft excesses previously in a few Seyfert spectra (Jin et al. 2009; Middleton et al. 2009). We also demonstrated that a single-temperature blackbody, despite providing a plausible phenomenological description of the soft excess in the time-averaged spectrum, cannot yield a satisfactory fit to the low-frequency σ_{rms} spectrum.

The soft excess varies independently of the hard power law; additional examples of this behavior in other Seyferts' X-ray spectra are given in e.g. Rivers et al. (2012); Markowitz et al. (2009) (although cases where the soft excess varies with the harder powerlaw have also been observed, e.g. 1H0707-495 (Fabian et al. 2009), IRAS 13224 3809 (Ponti et al. 2010)). The independent variability is evident in the low-frequency σ_{rms} spectrum, where only the soft excess appears, and in the higher frequency σ_{rms} spectra, where the powerlaw is present and the soft excess disappears. The power spectrum of the soft excess cannot be studied in detail since this component only exhibits a slow trend throughout the observation. The long-term *RXTE* light curves cannot provide additional information on the long term behavior of the soft excess since they only track energies above 2 keV.

The optical/UV light curves presented in Markowitz et al. (2009) show a steady increase in flux by $\sim 10\%$ throughout the observation, qualitatively similar to the increase seen in the soft X-rays (factor of ~ 2 increase throughout the observation). This behavior is consistent with a connected optical/UV/soft X-ray trend. It is not possible, however, to establish the significance of this correlation since the timescale of the trend is similar or longer than the duration of the observation, and it is not unlikely that uncorrelated trends on these timescales would look similar by chance.² A similar optical–soft X-ray correlation has been observed in Mkn 509 (Mehdipour et al. 2011). These authors find a soft X-ray excess and hard X-ray power law that each vary independently over timescales of a few days, but the addition of a simultaneous UV light curve shows that the soft excess does correlate well with the variability at lower energies. Mehdipour et al. interpret this soft excess as Comptonized thermal disc photons by a corona of optical depth $\tau \sim 17$ and electron temperature $k_{\text{B}}T_{\text{e}} \sim 0.2$ keV in the vicinity of the accretion disc. In our case, the variable (time-averaged) soft excess can be modeled as a Comptonized component with $\tau \sim 14$ (24) and $k_{\text{B}}T_{\text{e}} \sim 1.0$ (0.35) keV; importantly, the soft excess also displays uncorrelated variability to the hard power law and a closer connection to the optical/UV behavior. Therefore, a similar interpretation is warranted for the soft excess in NGC 3227. This interpretation of the origin of the soft excess emission was previously discussed in Markowitz et al. (2009) together with other observations of variable soft excesses.

As discussed in (Markowitz et al. 2009), the soft ex-

² In principle, the same argument applies to the slow variations of the soft X-ray energy bins, they could be uncorrelated narrow emission features that varied in the same way during the observation. Although such a spectral decomposition is not usual and the chance correlation of several bands is less likely, it is a possibility that cannot be ruled out.

cess in NGC 3227 doubles its flux on a timescale of 50 ks. This duration corresponds to a light travel time of $\sim 1000 R_g$, where $R_g \equiv GM_{\text{BH}}/c^2$, or ~ 10 times the orbital timescale at $6R_g$. This timescale might be too short for accretion rate fluctuations produced by viscous processes in the geometrically thin accretion disc, but might originate in a geometrically thick corona.

Finally, the low frequency σ_{rms} spectrum drops steeply with energy up to ~ 3 keV but it begins to rise again above this energy. The lack of correlation between low and high energy slow fluctuations argues against a single component for the whole low-frequency σ_{rms} spectrum. It is tempting to identify the higher-energy portion of the slowly-varying component with a Compton reflection hump varying on timescales of >30 ks (i.e., $1000 R_g/c$) and not on shorter timescales. Rivers et al. (2011) fit the time-averaged *RXTE* spectrum for this source using and measured only a very weak reflection hump (a value of reflection strength $R = 0.3 \pm 0.1$ using the PEXRAV model component), which would only account for approximately 3% of the total flux in the 6–10 keV band. Therefore, if the Compton hump were varying as much as the soft excess at low frequencies ($F_{\text{var}} = 6.7\%$), we would only expect a value of $F_{\text{var}} = 6.7\%/33 = 0.2\%$ in the 6.4–10 keV band, in contrast to the value observed, $F_{\text{var}} = 1.7\%$. The Compton hump therefore could produce only a small fraction of the slow variations in the hard bands, which are more likely produced by the power-law component.

Finally, we note that blurred, ionized reflection as a source for the soft excess did not fit well the spectrum of this source below 3 keV, so the low-frequency σ_{rms} spectrum does not correspond to a disc reflection component varying in normalization. In the disc reflection scenario, the high amplitude variation observed in the soft excess could be produced by changes in the ionization parameter instead, affecting mainly the line emission, below 2 keV. The powerlaw component did not vary on these long timescales during this observation, so the large change in ionization state could not have been produced by a similar change in illumination, unless it were responding to earlier fluctuations. The delay in the response of the disc reflection would have to be longer than the observation length, i.e. 100 ks, which equals the light travel time across several thousand gravitational radii in this AGN, making this scenario unlikely.

7.2. Rapidly-varying power-law component

The σ_{rms} spectrum of the rapid fluctuations in this observation has a power-law shape over the 0.2–10 keV range, affected by constant cold and warm absorption. The parameters of the absorbers are consistent with those measured in the time-averaged spectrum (M09) and in the slowly-varying soft excess. Similar σ_{rms} spectra have been observed in other Seyfert galaxies, e.g. MCG–6–30–15 (Papadakis et al. 2005) and Mkn 766 (Arévalo et al. 2008a), where the variability spectrum is approximately a power law with a broad absorption feature around 0.7–1 keV. This common feature in σ_{rms} spectra of Seyfert galaxies with soft excesses indicates that constant warm absorption acting on the power law component is present in all these sources. As shown

above, the spectrum of NGC 3227 has at least two separate continuum components, the soft-excess discussed in the previous section and a hard powerlaw. The warm absorption appears around the energies where these components intersect, modifying the time-average spectrum further.

The spectral variability of NGC 3227 as observed in the long term *RXTE* monitoring data presented by Uttley & McHardy (2005) indicated that pivoting of the hard power-law is the main source of flux variability in the 2–15 keV band. The pivot point was calculated to be at a few hundred keV. For energies far below the pivot point, the fluctuations resemble simple changes in normalization, but where the amplitude of variations increases with decreasing energy. The σ_{rms} spectrum expected from such a pivoting powerlaw is also a powerlaw but with slightly steeper slope, to account for the larger fluctuations at lower energies.

With this *XMM-Newton* observation we can study the spectral shape of this variable component down to lower energies. The coherence analysis for rapid (less than 30 ks) fluctuations indicates that the σ_{rms} spectrum corresponds to a single spectral component down to 0.2 keV. Its shape is a hard power law of $\Gamma \sim 1.75 - 1.85$. Markowitz et al. (2009) has fitted the time-averaged energy spectrum with several components including a power law to account for most of the hard band flux. The fitted slope in their ‘SXPL’ broadband model fit was $\Gamma = 1.57 \pm 0.02$, flatter than the σ_{rms} spectral slope and consistent with the pivoting scenario.

Uttley & McHardy (2005) find that the long term fractional variability (i.e. $\sigma_{\text{rms}}/\text{count rate}$) of NGC 3227 in the 3–5 keV band is 50% while in the 7–15 keV band it is 38%. For a time-averaged photon index Γ of 1.6, this dependence of fractional variability on energy band corresponds to an σ_{rms} spectrum with $\Gamma = 1.9$, similar to that observed in the *XMM-Newton* observations for the 0.2–10 keV band. The consistency between σ_{rms} slopes in the hard band for long term *RXTE* and short term *XMM-Newton* light curves argues for a single hard power-law component producing all the observed variability above 2 keV, while the low-frequency σ_{rms} spectrum with $\Gamma \sim 3$ in this *XMM-Newton* observation is produced by a separate spectral component.

Papadakis et al. (2007) constructed σ_{rms} spectra for six Seyfert galaxies and compared their slopes to the stellar-mass black hole X-ray binary (BHXR) Cyg X-1 in its hard and soft states (Revnivtsev et al. 1999; Gilfanov et al. 2000). They fit the spectra above 3 keV to characterize the slope of the variable hard power-law so we can only compare their results to the high-frequency σ_{rms} spectra of our *XMM-Newton* observation of NGC 3227. They find the six AGN σ_{rms} spectral slopes to lie between the hard and soft states of Cyg X-1 and become flatter with increasing frequency at a rate of $\Delta\Gamma \propto f^{-0.25}$. The comparison between objects of different black hole mass is facilitated by scaling the variability frequencies to the Keplerian frequency f_K of each object at 3 Schwarzschild radii. Using a black hole mass for NGC 3227 of $10^{6.88} M_\odot$ from Denney et al. (2010), our measurements for NGC 3227 fall slightly below the relation of Papadakis et al. (2007); at $f/f_K = 0.6$ we

measure a slope of 1.76 vs. 1.95 measured for other AGN and at $f/f_K = 0.12$ we find 1.87 vs. 2.3. The σ_{rms} slopes we measure do not depend as strongly on frequency as the composite of the sample of the other six AGN, with a $\Delta\Gamma \propto f^{-0.03}$ but the trend is at least in the same direction.

The accretion rate of NGC 3227 relative to Eddington was estimated by Vasudevan & Fabian (2009) from simultaneous *XMM-Newton* X-ray and optical/UV observations to be $L_{\text{bol}}/L_{\text{Edd}} = 0.45 - 1.5 \times 10^{-3}$. However, the black hole mass estimate from reverberation-mapping M_{BH} has since been revised from $10^{7.63} M_{\odot}$ (Peterson et al. 2004) to $10^{6.88} M_{\odot}$ (Denney et al. 2010), yielding $L_{\text{bol}}/L_{\text{Edd}} = 2.5 - 8.5 \times 10^{-3}$. Using *Swift*-BAT and *IRAS* observations (and the updated value of M_{BH}), Vasudevan et al. (2010) derive $L_{\text{bol}}/L_{\text{Edd}} = 2.0 - 3.9 \times 10^{-2}$. Even this corrected estimate of the accretion rate is significantly lower than the average of the six AGN in the Papadakis et al. (2007) sample of $L_{\text{bol}}/L_{\text{Edd}} = 0.65$ (Uttley & McHardy 2005, and reference therein). The high-frequency σ_{rms} spectra of NGC 3227 are flatter than those found for other AGN. These values of Γ do, however, fall between the values of the σ_{rms} spectral slopes of Cyg X-1 in soft and hard states, but closer to the hard state values than the other AGN investigated. Therefore, our results combined with those of Papadakis et al. (2007) are consistent with a picture where the σ_{rms} spectra flatten with decreasing accretion rate, both in AGN and in the BHXRB Cyg X-1.

As a final note, we recall the position of NGC 3227 within the plane describing the dependence of X-ray PDS break timescale $T_b \equiv 1/f_b$ on both M_{BH} and L_{Bol} , applicable to Seyfert AGN and BH XRBs simultaneously, and empirically quantified by McHardy et al. (2006). Using the updated value for the black hole mass estimate and using the values of L_{Bol} reported by Vasudevan et al. (2010), $10^{43.2-43.5} \text{ erg s}^{-1}$, the empirical relation of McHardy et al. (2006) (using the best-fit values for the coefficients and ignoring the coefficient uncertainties for the moment) yields predictions for T_b of 1.04–2.05 d, completely consistent with our measured value of $T_b = 1.01^{+2.39}_{-0.50}$ d. For completeness, using values of L_{Bol} from Woo & Urry (2002; $10^{43.9} \text{ erg s}^{-1}$), as was done by UM05, or Vasudevan & Fabian (2009) ($10^{42.4-42.9} \text{ erg s}^{-1}$) instead yields predictions for T_b of 0.42 d or 4.1–12.5 d, respectively.

8. CONCLUSIONS

We studied the energy- and temporal-frequency-dependent behavior of the X-ray continuum emission components in the Seyfert 1.5 AGN NGC 3227 using a 100 ks long-look obtained with *XMM-Newton* in 2006.

We revisited the broadband 2–10 keV PDS of this source, first published by UM05, by combining the PDS derived from the *XMM-Newton* light curve with PDS derived from multi-timescale *RXTE* monitoring. We applied a bending power-law model, and obtained a best-fit bend frequency of $1.15^{+0.76}_{-0.81} \times 10^{-5} \text{ Hz}$ ($1.01^{+2.39}_{-0.40}$ d), consistent with the results of UM05 and consistent with the empirical relation between X-ray black hole mass, and X-ray luminosity of McHardy et al. (2006) considering

updated measurements of the black hole mass.

The *XMM-Newton* observation coincided with a period of low variability amplitude above 2 keV on timescales of 50–100 ks. This chance occurrence allowed us to identify a separate soft component varying slowly in normalization, and independently of variations in the coronal hard X-ray power-law component. More specifically, the timescale-resolved σ_{rms} spectra together with the coherence analysis allowed us to isolate and quantify the variable components: the steep soft excess varying coherently from 0.2 up to 2 keV and dominating the variability on timescales longer than 30 ks, and the harder power-law component, varying coherently from 0.2–10 keV and dominating the variability on timescales shorter than 30 ks.

Both components are affected to the same extent as the time-averaged spectrum by absorption by full-covering, neutral and ionized gas along the line of sight. The cold and warm absorbers are constant on timescales covered by this observation and the variability is intrinsic to the emitting regions.

The variable soft excess component can be well-described by a steep ($\Gamma \sim 3$) power-law. It can also be described by a model of thermal Comptonization, in which optical/UV seed photons are upscattered by a distribution of hot electrons with optical depth $\sim 14 - 24$ and electron temperature $k_B T \sim 0.3 - 1 \text{ keV}$. A blackbody component, despite being an acceptable phenomenological fit to the soft excess in the time-averaged spectrum, is ruled out by the σ_{rms} spectra, as is a blurred ionized reflection component.

The σ_{rms} spectrum of the hard power law has a slope of $\Gamma \sim 1.8$, similar to but steeper than the power law fitted to the time-averaged spectrum. This steepening is consistent with the pivoting mechanism proposed to model the hard X-ray variability of this object from long-term light curves in the 2–15 keV band (Uttley & McHardy 2005). The hard power-law variability is not well-correlated with either the soft excess or optical/UV fluctuations on the time-scales studied, 5–100 ks, which supports the division of the X-ray spectrum in at least two emission components. The rapid fluctuations that characterize the powerlaw component show hard lags at a level of 2% of the variability timescale, in line with similar findings of powerlaw variability in other AGN. A longer monitoring campaign would be needed to test whether the optical/soft X-ray and hard X-ray bands are correlated on long timescales, as is often the case in other Seyfert galaxies.

ACKNOWLEDGEMENTS

This work is based on observations obtained with *XMM-Newton*, an ESA science mission with instruments and contributions directly funded by ESA Member States and NASA and has made use of HEASARC online services, supported by NASA/GSFC, the NASA/IPAC Extragalactic Database, operated by JPL/California Institute of Technology under contract with NASA, and the NIST Atomic Spectra Database. PA acknowledges financial support from Fondecyt grant 11100449 and Anillo ACT1101.

REFERENCES

- Arévalo, P., Churazov, E., Zhuravleva, I., Hernández-Monteagudo, C., & Revnivtsev, M. 2012, *MNRAS*, 426, 1793
- Arévalo, P., McHardy, I. M., Markowitz, A., et al. 2008a, *MNRAS*, 387, 279
- Arévalo, P., McHardy, I. M., & Summons, D. P. 2008b, *MNRAS*, 388, 211
- Arévalo, P., Papadakis, I. E., Uttley, P., McHardy, I. M., & Brinkmann, W. 2006, *MNRAS*, 372, 401
- Crummy, J., Fabian, A. C., Gallo, L., & Ross, R. R. 2006, *MNRAS*, 365, 1067
- de Vaucouleurs, G., & et al. 1991, *Third Reference Catalogue of Bright Galaxies, Version 3.9*, 365
- Denney, K. D., Peterson, B. M., Pogge, R. W., et al. 2010, *ApJ*, 721, 715
- Fabian, A. C., Zoghbi, A., Ross, R. R., et al. 2009, *Nature*, 459, 540
- Gierliński, M., & Done, C. 2004, *MNRAS*, 349, L7
- Gilfanov, M., Churazov, E., & Revnivtsev, M. 2000, *MNRAS*, 316, 923
- Haardt, F., & Maraschi, L. 1991, *ApJL*, 380, L51
- Jin, C., Done, C., Ward, M., Gierliński, M., & Mullaney, J. 2009, *MNRAS*, 398, L16
- Kalberla, P. M. W., Burton, W. B., Hartmann, D., et al. 2005, *A&A*, 440, 775
- Markowitz, A., Reeves, J. N., George, I. M., et al. 2009, *ApJ*, 691, 922
- Markowitz, A., & Uttley, P. 2005, *ApJL*, 625, L39
- Markowitz, A., Edelson, R., Vaughan, S., et al. 2003, *ApJ*, 593, 96
- McHardy, I. M., Papadakis, I. E., Uttley, P., Page, M. J., & Mason, K. O. 2004, *MNRAS*, 348, 783
- Mehdipour, M., Branduardi-Raymont, G., Kaastra, J. S., et al. 2011, *A&A*, 534, A39
- Middleton, M., Done, C., Ward, M., Gierliński, M., & Schurch, N. 2009, *MNRAS*, 394, 250
- Papadakis, I. E., Ioannou, Z., & Kazanas, D. 2007, *ApJ*, 661, 38
- Papadakis, I. E., Kazanas, D., & Akylas, A. 2005, *ApJ*, 631, 727
- Papadakis, I. E., Nandra, K., & Kazanas, D. 2001, *ApJL*, 554, L133
- Peterson, B. M., Ferrarese, L., Gilbert, K. M., et al. 2004, *ApJ*, 613, 682
- Ponti, G., Gallo, L. C., Fabian, A. C., et al. 2010, *MNRAS*, 406, 2591
- Revnivtsev, M., Gilfanov, M., & Churazov, E. 1999, *A&A*, 347, L23
- Rivers, E., Markowitz, A., Duro, R., & Rothschild, R. 2012, *ApJ*, 759, 63
- Rivers, E., Markowitz, A., & Rothschild, R. 2011, *ApJS*, 193, 3
- Ross, R. R., & Fabian, A. C. 2005, *MNRAS*, 358, 211
- Strüder, L., Briel, U., Dennerl, K., et al. 2001, *A&A*, 365, L18
- Sunyaev, R. A., & Titarchuk, L. G. 1980, *A&A*, 86, 121
- Turner, T. J., & Pounds, K. A. 1989, *MNRAS*, 240, 833
- Uttley, P., & McHardy, I. M. 2005, *MNRAS*, 363, 586
- Uttley, P., McHardy, I. M., & Papadakis, I. E. 2002, *MNRAS*, 332, 231
- Vasudevan, R. V., & Fabian, A. C. 2009, *MNRAS*, 392, 1124
- Vasudevan, R. V., Fabian, A. C., Gandhi, P., Winter, L. M., & Mushotzky, R. F. 2010, *MNRAS*, 402, 1081
- Vaughan, S., Edelson, R., Warwick, R. S., & Uttley, P. 2003, *MNRAS*, 345, 1271
- Walton, D. J., Zoghbi, A., Cackett, E. M., et al. 2013, *ApJL*, 777, L23